Inorganic Chemistry

ARTICLE

pubs.acs.org/IC

Exchange Interactions Through $\pi-\pi$ Stacking in the Lamellar Compound $[\{Cu(bipy)(en)\}\{Cu(bipy)(H_2O)\}\{VO_3\}_4]_n$

Diego Venegas-Yazigi,[*,†,‡] Kareen A. Brown,[‡,§] Andrés Vega,[‡,▽] Rafael Calvo,[⊥] Carolina Aliaga,[†,‡] Ricardo C. Santana,[∥] Raul Cardoso-Gil,[○] Rüdiger Kniep,[○] Walter Schnelle,[○] and Evgenia Spodine[*,‡,§]

[†]Facultad de Química y Biología, Universidad de Santiago de Chile, USACH, Santiago, Chile

[‡]Centro para el Desarrollo de Nanociencias y Nanotecnología, CEDENNA, Santiago, Chile

[§]Facultad de Ciencias Químicas y Farmacéuticas, Universidad de Chile, Santiago, Chile

[▽]Departamento de Ciencias Químicas, Universidad Andres Bello, Santiago, Chile

[⊥]Facultad de Bioquímica y Ciencias Biológicas and INTEC, CONICET-Universidad Nacional del Litoral, 3000 Santa Fe, Argentina

[∥]Instituto de Física, Universidade Federal de Goiás, CP 131, 74001-970 Goiânia, Brazil

[○]Max-Planck-Institut für Chemische Physik fester Stoffe, Dresden, Germany

Supporting Information

ABSTRACT:

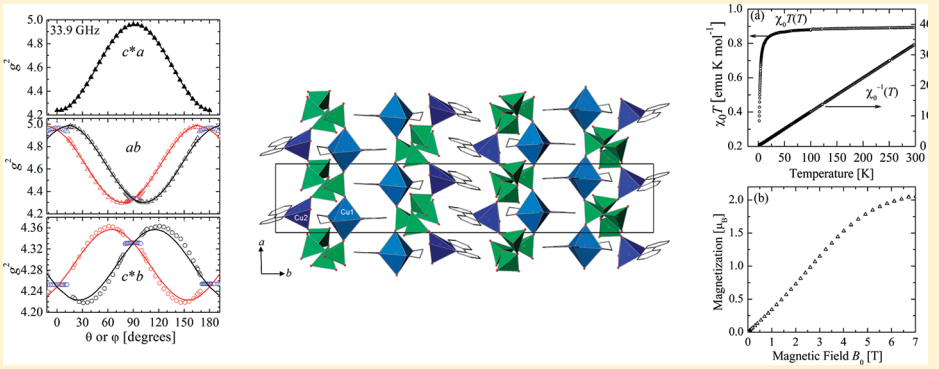

Structural, magnetic, and powder and single-crystal electron paramagnetic resonance (EPR) studies were performed on $[\{Cu(bipy)(en)\}\{Cu(bipy)(H_2O)\}\{VO_3\}_4]_n$ (bipy = 2,2′-bipyridine, en = ethylenediamine), which is a new copper−vanadium hybrid organic−inorganic compound containing Cu^{II} and V^{V} centers. The oxovanadium units provide an anionic scaffolding to the structure, where two types of Cu^{II} coordination modes, octahedral (Cu1) and square pyramidal (Cu2), contribute to the magnetic properties. The crystal structure contains layers including Cu1 and Cu2 ions, separated by stacked arrangements of 2,2′-bipyridine molecules. Each type of Cu^{II} ion in these layers forms parallel spin chains described by exchange coupling parameters J_1 and J_2 for Cu1 and Cu2, respectively (exchange couplings defined as $\mathcal{H}_{ex}(i,j) = -J_{ij}\,\boldsymbol{S}_i\boldsymbol{S}_j$), which, for necessity, are assumed to be equal to J. These chains are coupled by much weaker Cu1−Cu2 exchange interactions J_3 connecting neighbor Cu1 and Cu2 ions within a layer, through paths acting as rungs of a ladder chain structure. The average coupling J, which is antiferromagnetic ($J < 0$), according to the susceptibility data, is estimated with similar results with a mean field approximation ($J = -1.4$ cm^{-1}), and with a uniform chain model ($J = -1.7$ cm^{-1}). The EPR spectra of powdered samples and oriented single crystals are shown to be independent of J_1 and J_2, but are dependent on the weak coupling J_3, and the data allow a lower limit to be established: $|J_3| > 0.04$ cm^{-1}. The spectra are also strongly sensitive to extremely weak coupling interactions with average magnitude J_4 between copper atoms in neighboring layers, separated by ∼10 Å, using the stacked 2,2′-bipyridine molecules, which produce a 2D-to-3D quantum phase transition. This is observed in single-crystal samples when the energy levels are changed with the orientation of the magnetic field. From the characteristics of these transitions, we estimate a value of $|J_4| = 0.0034 \pm 0.0004$ cm^{-1} between Cu^{II} ions in neighboring layers. This work emphasizes the important possibilities of EPR to evaluate extremely small exchange couplings between metal ions in a solid material, even in the presence of other much larger couplings.

Received: June 14, 2011
Published: October 25, 2011

INTRODUCTION

Vanadium oxides, which represent a subset of inorganic oxides, have been investigated in recent decades with respect to their structural diversity, forming various types of structures, such as clusters, infinite chains, layers, and multidimensional frameworks. Complex oxovanadates contain anionic partial structures $\{V_xO_y\}^{n-}$ ranging from monomeric $[VO_4]^{3-}$ units, to oligomers and clusters ($[V_2O_7]^{4-}$, $[V_4O_{12}]^{4-}$, $[V_6O_{18}]^{6-}$, $[V_{10}O_{28}]^{6-}$), to $[VO_3]_n^{n-}$ chains, and $[V_xO_y]^{n-}$ networks.[1−3] An organic component, such as a nitrogen donor ligand, may be introduced to a secondary metal site, which, in turn, influences the range of binding interactions with the oxide skeleton.[4−7] Many recent papers and reviews have highlighted the rich and subtle chemistry found in hybrid polyoxovanadate-based compounds prepared using hydrothermal techniques.[8−10] Several reports found in the literature involve vanadate compounds functionalized with Cu^{II} complexes.[11−13] The rapid progress of exploring copper-containing organic−inorganic hybrid materials[8−11,13−26] is driven by their interesting structures and properties, with applications to ion exchange, sorption, catalysis, electrical conductivity, photochemistry, and magnetism.

This paper reports the hydrothermal synthesis, and the structural, magnetic and electron paramagnetic resonance (EPR) spectra characterization of a new hybrid organic−inorganic compound $[\{Cu(bipy)(en)\}\{Cu(bipy)(H_2O)\}\{VO_3\}_4]_n$ (**1**), where bipy is 2,2′-bipyridine, and en is ethylenediamine. Two different Cu^{II} coordination compounds functionalizing the vanadate framework are arranged in layers, separated by bipy rings (distance of ca. 10 Å). Since the V^V ions do not carry unpaired electronic spins, the magnetic properties of **1** are mainly a consequence of the Cu^{II} ions, with the V^V ions within the diamagnetic chemical paths supporting the super exchange interactions between copper atoms. Susceptibility and magnetization data allow estimation of the average exchange interactions between neighboring copper ions within the layers. Powder and single-crystal EPR measurements display a remarkable low-dimensional magnetic behavior with much weaker interactions between Cu^{II} spins in neighboring layers, transmitted by the $\pi-\pi$ stacking of the bipy moieties. These interactions lead to a stochastic distribution of dynamical local fields, producing a temperature-independent quantum phase transition, which is observed as sudden changes in the EPR spectra when the level scheme is varied with the magnetic field orientation.[27−31] This transition provides a way to estimate the weak exchange interactions between the Cu^{II} centers in adjacent layers supported by the stacking of the bipy rings. Aromatic ring stacking is important in chemistry and biology[32,33] and may support extremely weak exchange interactions between unpaired spins. The characterization of these interactions is difficult, because they normally coexist with other stronger ones. Measuring weak exchange couplings through biologically relevant noncovalent bonds, such as ring stacking, may be helpful to estimate matrix elements for electron transfer in proteins and model systems.[34] Estimations of exchange couplings supported by aromatic ring stacking have been reported in the past.[32,35−37] Most of these calculations evaluate the exchange parameters from susceptibility data using the molecular field approximation, offering only modest possibilities to separate the effects of interactions of different types and magnitudes, contributing to the bulk magnetic properties. As presented in this work, EPR studies are much more appropriate for this purpose. The single-crystal EPR experiments analyzed considering the space symmetry properties of the compound, allow evaluation of the interlayer exchange interactions from quantum effects observed in the spectra, as a consequence of the weak coupling interactions between copper atoms in neighboring layers supported by the stacking of the bipy rings. To the best of our knowledge, this is the first EPR study performed on a single crystal of an oxovanadium-based organo-inorganic hybrid material functionalized with Cu^{II} complexes.

EXPERIMENTAL SECTION

Synthesis of $[\{Cu(bipy)(en)\}\{Cu(bipy)(H_2O)\}\{VO_3\}_4]_n$ (1). The reaction mixture of NH_4VO_3 (1.85×10^{-3} mol, 0.217 g), $Na_2B_4O_7 \cdot 10H_2O$ (4.94×10^{-3} mol, 1.890 g), $Cu(NO_3)_2 \cdot 3H_2O$ (1.85×10^{-3} mol, 0.448 g), ethylenediamine (1.24×10^{-3} mol, 80 μL), 2,2′-bipyridine (1.85×10^{-3} mol, 0.290 g), and 1.5 mL H_2O was heated in a 23-mL Teflon-lined Parr reactor at 120 °C for 72 h. After the reactor was cooled to room temperature, blue crystals of the product were isolated, washed with water, and dried at room temperature (yield: 90%, 0.382 g).

The infrared spectrum of **1** shows the bands of the 2,2′-bipyridine ligand between 1598(s) and 1243(s) cm^{-1}, and the bands associated with the ethylenediamine ligand at 1624(m), 1158(m), 1116(s), and 1028(m) cm^{-1}. Four additional bands, at 924(vs), 825(m), 784(vs), 645(sh) cm^{-1}, are assigned to asymmetric and symmetric (V−O−V) stretching modes.

Single-Crystal X-ray Diffraction. The crystal structure of **1** was determined at 298 K by X-ray diffraction on a needle-shaped single crystal with dimensions of 0.43 mm × 0.08 mm × 0.07 mm. Data collection was done on a SMART CCD diffractometer, using ω-scans. Data reduction was done with SAINT,[38] while the structure was solved by direct methods; completion and refinement was conducted with SHELXL.[39] Empirical absorption corrections were applied using SADABS.[40] The positions of the hydrogen atoms were calculated after each cycle of refinement with SHELXL using a riding model for each structure, with bond distances of C_{sp3}—H = 0.97 Å, C_{arom}—H = 0.93 Å, N−H = 0.90 Å, and O−H = 0.92 Å. U_{iso}(H) values were set to $1.2U_{eq}$ of the parent carbon or nitrogen atom and $1.5U_{eq}$ of the parent oxygen. One of the two aqua hydrogen atoms was located in the difference Fourier map and refined with constraints, while the second one was not confidently located. During the final stages of refinement, disorder of the position of oxygen atoms O2 and O3 was noticed. It was modeled proposing two positions *p* and *q* for both atoms, with the occupancies being subsequently refined and subjected to the condition to sum up to one. This procedure converged to occupancies of 0.79 and 0.21, which were held constant during the last stages of refinement. Crystallographic data, as well as details on data collection and refinement, are given in Table 1.

Magnetic Measurements. The magnetization of the samples was measured with a SQUID magnetometer (MPMS XL7, Quantum Design) at magnetic fields of B_0 = 0.04, 0.2, and 1 T ($B_0 = \mu_0 H$, where μ_0 is the permeability of the vacuum) and at temperatures between T = 1.8 and T = 300 K. In addition, an isothermal magnetization curve up to B_0 = 7 T was measured at 1.8 K. The magnetic susceptibility data were corrected for diamagnetism and TIP, estimated at each field from the χ vs $1/T$ plots and giving values of 6.92, 4.70, and 3.64×10^{-4} emu, at B_0 = 0.04, 0.2, and 1 T, respectively. These values agree with that expected according to the current literature.[41] The contribution from the sample holder was measured independently and subtracted from the data.

EPR Measurements. EPR spectra from powdered samples, obtained by grinding single crystals, were collected at room temperature using a Bruker Model ESP-300 spectrometer working at 33.78 and 9.60 GHz with a rotating magnet, and a Bruker Model EMX-1572 spectrometer operating at 9.8 GHz, both using microwave cavities operating with a magnetic field modulation of 100 kHz. At 33.92 GHz, we also

dx.doi.org/10.1021/ic201278a |*Inorg. Chem.* 2011, 50, 11461–11471

collected the spectra of a single crystal, as a function of the orientation of the magnetic field. The single crystal was oriented by gluing an *ac* ([010]) growth face to a cleaved cubic KBr single crystal holder, with the ***a***-axis in parallel orientation to one of the sides of the holder, which defined a system ***xyz*** of orthogonal axes, with ***x*//*a***, ***y*//*b***, ***z*//*c**, where $\boldsymbol{c}^* = \boldsymbol{a} \times \boldsymbol{b}$.[42] The spectra of the single crystals were recorded at ∼5° orientation intervals of the applied field $\boldsymbol{B}_0 = B_0[\sin\theta\cos\phi, \sin\theta\sin\phi, \cos\theta]$ (where θ and ϕ are, respectively, the polar and azimuthal angles of the magnetic field direction), in a range of 180° of the crystal planes *ab*, *c***b*, and *c***a*. The amplitude of the 100 kHz field modulation was chosen to be between 0.05 mT and 0.1 mT, and the microwave power was 33 and 10 mW at 33.92 and 9.60 GHz, respectively. The magnetic field at the position of the sample was calibrated using DPPH (g = 2.0036) as a field marker. The orientations of the ***a***-, ***b***-, and ***c****-axes in the *ab* and *c***b* crystal planes were located within 1°, considering the symmetry properties of the ***b***-axis. The ***a***- and ***c****-axes in the *c***a* plane were located, considering the values obtained within the three planes. For EPR spectra simulations and fittings, the EasySpin[43] program package, working under Matlab, was used.[44]

Table 1. Crystal Data and Structure Refinement for $[\{Cu(bipy)(en)\}\{Cu(bipy)(H_2O)\}\{VO_3\}_4]_n$

parameter	value
formula weight, FW	912.34 amu
crystal system	monoclinic
space group	$P2_1/n$
a	7.2700(2) Å
b	39.8343(11) Å
c	10.5923(3) Å
β (°)	97.9510(10)
volume, V	3037.99(15) Å^3
Z (Z')	4
ρ	1.995 g cm^{-3}
μ	2.629 mm^{-1}
F(000)	1812.0
θ range	2.01°−25.00°
hkl range	$-8 \le h \le 8$
	$-47 \le k \le 46$
	$-12 \le l \le 12$
N_{tot}, N_{uniq}	12348, 5359
(R_{int}), N_{obs}	(0.0382), 4542
refine parameters	443
goodness of fit, GOF	1.062
$R1$, $wR2$ (obs)	0.036, 0.083
$R1$, $wR2$ (all)	0.045, 0.088
Max. min $\Delta\rho$	0.515−0.388 e Å^{-3}

RESULTS

Structural Description of $[\{Cu(bipy)(en)\}\{Cu(bipy)(H_2O)\}\{VO_3\}_4]_n$ (1). The crystal structure of **1** contains infinite chains of $\{(VO_3)^-\}_n$ running along the ***c***-cell axis ([001]) (see Figure 1). These contain V^V, and formally alternate VO_2^+ and μ_2-O^{2-} oxo units, with torsion angles of O−V−O−V within the chain, which are summarized in Table 2. The chains are connected to $\{Cu1(bipy)(H_2O)\}^{2+}$ and $\{Cu2(bipy)(en)\}^{2+}$ units (distance of ca.

Table 2. Selected Bond and Interatomic Distances, Bond Angles, and Torsion Angles for Compound 1[a]

Bond Distances (Å)			
Cu1−N1	2.006(3)	Cu1−N4	2.013(3)
Cu1−N2	2.023(3)	Cu1−O1	2.309(3)
Cu1−N3	2.030(3)	Cu1−O3P^i	2.374(13)
Cu2−O8	2.235(2)	Cu2−N5	1.999(3)
Cu2−O12	1.949(2)	Cu2−N6	2.041(3)
Cu2−O1w	1.994(3)		
Interatomic Distances (Å)			
Cu1···Cu2	6.796(1)	Cu1···Cu1^{ii}	7.270(1)
Cu2···Cu2^{ii}	7.270(1)	Cu1···Cu1^{iii}	10.592(1)
Cu1···Cu1^{iii}	10.592(1)		
Bond Angles (deg)			
N1−Cu1−N2	80.94(12)	N1−Cu1−O1	88.21(12)
N1−Cu1−N3	96.03(12)	N2−Cu1−O1	93.69(12)
N1−Cu1−N4	174.95(12)	N3−Cu1−O1	93.32(12)
N2−Cu1−N3	172.27(12)	N4−Cu1−O1	86.77(12)
N4−Cu1−N2	98.81(12)	N1−Cu1−O3P^i	88.0(6)
N4−Cu1−N3	84.84(12)	N2−Cu1−O3P^i	89.3(8)
N3−Cu1−O3P^i	83.5(8)	N4−Cu1−O3P^i	97.0(6)
N5−Cu2−N6	80.23(11)	O12−Cu2−N5	90.78(11)
N5−Cu2−O8	92.98(10)	O12−Cu2−N6	155.17(12)
N6−Cu2−O8	97.07(10)	O12−Cu2−O8	106.54(11)
O1−Cu1−O3B^i	174.8(6)	O12−Cu2−O1w	88.64(13)
O1w−Cu2-N5	175.77(13)	O1w−Cu2−N6	98.63(13)
Torsion Angles (deg)			
O6−V2−O4−V1	77.8(3)	O2p−V1−O4−V2	166.5(3)
O9−V3−O6−V2	39.4(2)	O6−V3−O9−V4	147.02(19)

[a] Symmetry codes: i = 1 + x, y, z, ii = −1 + x, y, z, and iii = x, y, 1 + z.

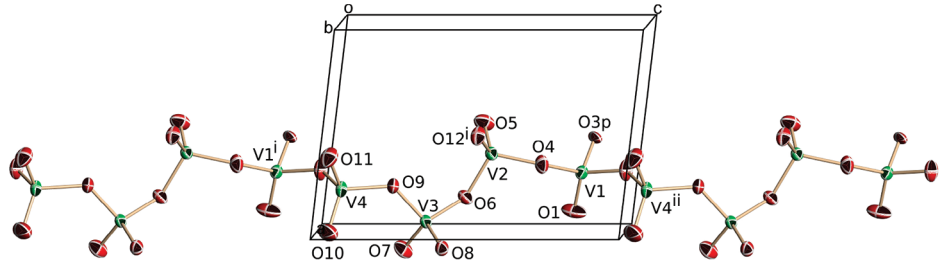

Figure 1. Infinite $\{(VO_3)^-\}_n$ chains running along the [001] direction; displacement ellipsoids are at the 50% probability level. Symmetry labels: i: x, y, z − 1; ii: x, y, z + 1.

dx.doi.org/10.1021/ic201278a |*Inorg. Chem.* 2011, 50, 11461–11471

Cu1···Cu2 = 6.796 Å), acting as covalent linkers. Coordination spheres around Cu1 and Cu2 are completed by two oxygen atoms from the chain (see Figure 2), leading to a *trans*-octahedral environment for Cu1, and to a distorted square base pyramid for Cu2 (τ = 0.34). The vanadyl oxygen atoms occupy the apical position (O8) and one of the basal positions (O12) of Cu2.

The unit cell contains four rotated Cu1 plus Cu2 units, positioned in four consecutive "rugous" layers parallel to the *ac* plane, at $y = {}^{1}/_{8}b$, ${}^{3}/_{8}b$, ${}^{5}/_{8}b$, and ${}^{7}/_{8}b$, labeled A, B, C and D, as depicted in Figure 3 (interlayer distances = $b/4 \approx 10$ Å). Bipyridine molecules from both cupric sites are approximately perpendicular to the CuVO layers, separating them.

The heterometallic oxide network displays two distinct cyclic submotifs, shown in Figure 4: a 14-membered $\{Cu_2V_5O_7\}$ ring (labeled I in Figure 4) and a 18-membered $\{Cu_2V_7O_9\}$ ring (labeled II in Figure 4) with dimensions of ca. 8.2 × 7.8 Å and ca. 8.5 × 9.9 Å, respectively. In contrast to the bipy molecules, which are almost perpendicular to the layer, the ethylenediamine ligands lie inside the layers. The minimum distance between copper centers of the same geometry (1−1 and 2−2) in the same layer is ca.7.270 Å (equal to the *a*-cell parameter) (see Figure 4).

The $\pi-\pi$ interactions between adjacent bipy rings promote the interconnection of neighbor parallel layers, generating a three-dimensional structure. There are two types of $\pi-\pi$ stacking, that of the bipy rings associated to hexacoordinated copper atoms (Cu1); and that of the bipy rings of pentacoordinated copper atoms (Cu2). Checking the values of the interplanar and centroid to centroid distances, 3.580 and 3.696 Å for the first type, and 3.362 and 3.631 Å for the second, it is possible to assume that the second interaction is more intense in magnitude than the first. Moreover, just one pair of pyridine rings is implied in the first interaction, while the complete bipy ligand is implied in the second one. Also, the overlap of the pyridine rings along the [100] for the first interaction is almost complete, while it is partial for the second one, as reflected by the slippage angles (14.4° and 22.2°, respectively; see Figure 5). This is reflected by the C−H···O oxo group, which further contributes to the interlayer stabilization. Table 3 summarizes the most relevant noncovalent interactions: H-bonds and $\pi-\pi$ stacking.

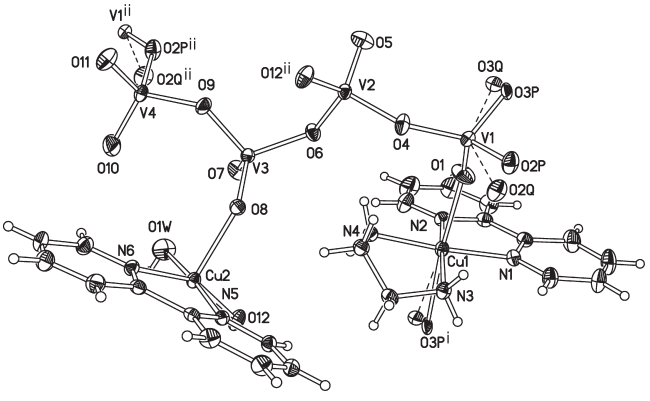

Figure 2. Octahedral $\{Cu(bipy)(en)\}^{2+}$ and square pyramidal $\{Cu(en)(H_2O)\}^{2+}$ cupric units connected to the infinite $\{(VO_3)^-\}_n$ chains via common oxygen sites. Symmetry labels: $i = x, y, z - 1$; $ii = x, y, z + 1$. Dashed bonds are used for disordered positions *p* and *q* for oxygen atoms O2 and O3.

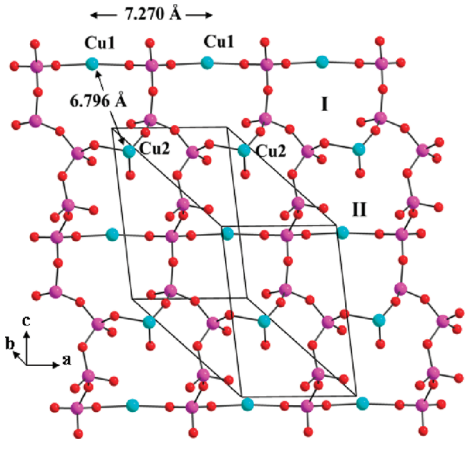

Figure 4. View of the layered structure of **1**, displaying the two distinct cyclic submotives connecting Cu1 and Cu2 neighboring ions in a layer: a 14-membered $\{Cu_2V_5O_7\}$ ring (I), and an 18-membered $\{Cu_2V_7O_9\}$ ring (II). Only copper (light blue), vanadium (magenta), and oxygen atoms (red) are shown.

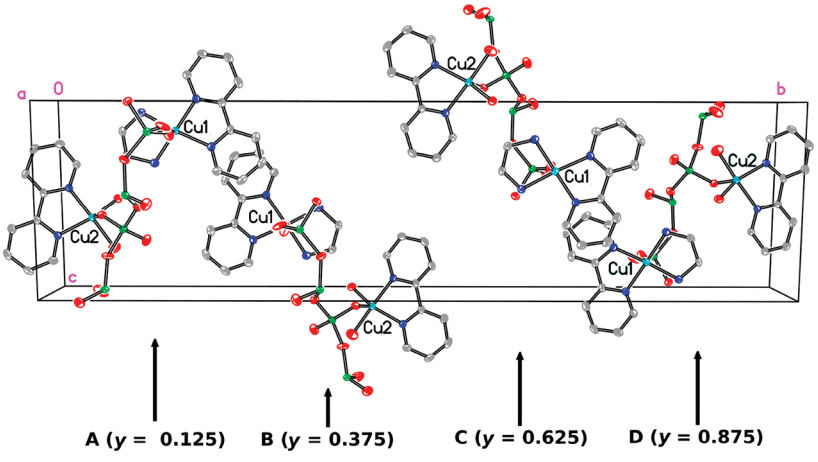

Figure 3. The eight sites in the unit cell of $[\{Cu(bipy)(en)\}\{Cu(bipy)(H_2O)\}\{(VO_3)_{4n}\}]_n$ (**1**), belonging to four consecutive 2-D layers, labeled A, B, C, and D.

dx.doi.org/10.1021/ic201278a |*Inorg. Chem.* 2011, 50, 11461–11471

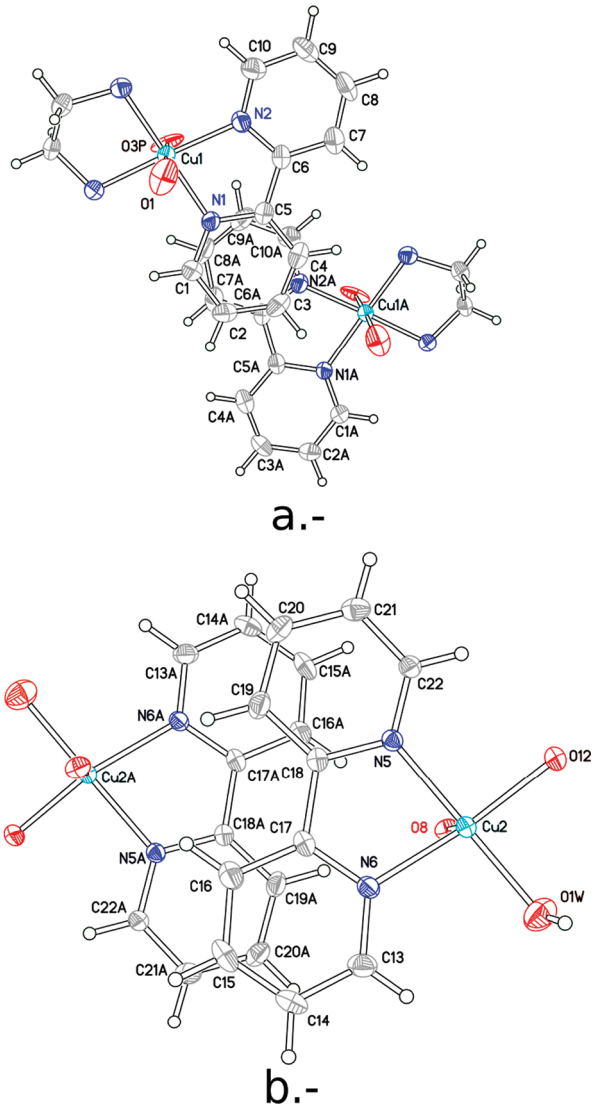

Figure 5. Overlap between the bipyridine rings for stacking interactions: (a) octahedral Cu1, $Cg^1 \cdots Cg^2$ $(1 + x, 1 - y, 1 + z)$ and (b) square pyramidal Cu2, $Cg^3 \cdots Cg^4$ $(-x, -y, 1 - z)$. Cg^1: N1, C1, C2, C3, C4, C5; Cg^2: N2, C6, C7, C8, C9, C10; Cg^3: N5, C18, C19, C20, C21, C22; and Cg^4: N6, C13, C14, C15, C16, C17.

Superexchange Pathways. The magnetic network of **1** can be described as two different spin chain arrangements along the *a*-axis [100], forming a 2D magnetic structure. The first chain contains octahedrally coordinated Cu1, with ca. 7.270 Å between adjacent spin carriers. The second chain contains pentacoordinated Cu2, at the same distance. Neighboring copper atoms in each type of chain are coupled by exchange interactions with magnitudes J_1 and J_2, respectively. In the case of Cu1 chains, the path for J_1 involves four covalent bonds between the two metal centers (Cu1−O−V−O−Cu1), while for J_2 six covalent bonds connect Cu2 neighboring ions in the chains, (Cu2−O−V−O−V−O−Cu2) (see Figure 4). Even when the linear distances between Cu1 and Cu2 type ions are the same, the distance through the bond (d_b) is longer for the path between the Cu2 ions. The closest Cu1 and Cu2 neighboring ions are at ca. 6.796 Å and the chemical path involves eight bonds and three V ions, and the corresponding interaction will be called J_3. In summary, the

Table 3. Hydrogen Bonds and $\pi-\pi$ Contacts for Compound 1 (Å and deg)[a]

D−H···A	d(D···A)
O1W−H1AW···O9^{i}	3.066(4)
N3−H3A···O2P^{i}	3.216(6)
N3−H3B···O10^{ii}	3.120(5)
N4−H4A···O6	3.175(4)
N4−H4B···O5^{i}	3.072(4)
C1−H1···O7^{ii}	3.135(5)
C3−H3···O1^{iii}	3.222(5)
C3−H3···O3P^{iii}	3.246(13)
C7−H7···O6^{iii}	3.453(5)
C11−H11B···O4^{i}	3.438(5)
C12−H12A···O8	3.356(5)
C12−H12B···O4	3.488(5)
C19−H19···O8^{iv}	3.447(5)
C20−H20···O11^{iv}	3.330(5)
C21−H21···O1^{v}	3.383(5)
C22−H22···O12	2.973(4)

[a] Symmetry codes: $i = 1 + x, y, z$; $ii = x, y, z + 1$; $iii = {}^1/_2 - x, {}^1/_2 - y, {}^3/_2 + z$; $iv = -x, -y, 1 - z$; $v = x + 1, y, 1 + z$.

coupling interactions and the relevant chemical paths connecting neighboring copper ions within a layer and between neighboring layers are given as

- J_1 → Cu1−Cu1 connected by axial−axial bridges Cu1−O−V−O−Cu1 (identical, nonrotated Cu1), with d_b ca. 7.943 Å.
- J_2 → Cu2−Cu2 connected by axial−equatorial bridges Cu2−O−V−O−V−O−Cu2 (identical, nonrotated Cu2), with d_b ca. 11.124 Å.
- J_3 → Cu1−Cu2 connected by axial−axial bridges Cu1−O−V−O−V-O−V−O−Cu2 with d_b ca. 15.107 Å.
- J_4 → Cu ions in neighboring layers at ca. 10 Å connected by complex, noncovalent arrays of bipyridine molecules.

The topology of the intrachain bridges between Cu1 and Cu2 ions having similar lengths, suggests that the magnitude $|J_1|$ is similar to $|J_2|$, since the larger number of bonds and bond length d_b of the Cu2 chains is compensated by its equatorial−apical character, compared with the apical−apical character for Cu1 chains. However, the magnitude of $|J_3|$ should be smaller than $|J_1|$ and $|J_2|$, because of the longer length and complexity of the corresponding paths. Since no covalent bonds are involved, the magnitude $|J_4|$ of the interlayer coupling interactions should be much weaker than $|J_1|$, $|J_2|$, and $|J_3|$.

While the chemical paths supporting J_1, J_2, and J_3 are well-defined, this is not the case for J_4. For the latter interaction, a Cu^{II} ion in one layer interacts with many Cu^{II} ions in the neighboring layer, through paths having similar lengths but a distribution of complexities. With regard to the effects of these interactions on the EPR spectra, the distribution of couplings around an average value is equivalent to a simple coupling. Our experiments allow evaluation of this average or "effective" value. As described previously and displayed in Figures 5 and 6, it should be emphasized that there are two types of ring stacking alternating in the structure, that could support the superexchange interactions between Cu ions in neighboring layers. The EPR measurements cannot discern between one and the other as being responsible for J_4, because both produce the same effect. In view

dx.doi.org/10.1021/ic201278a |*Inorg. Chem.* 2011, 50, 11461–11471

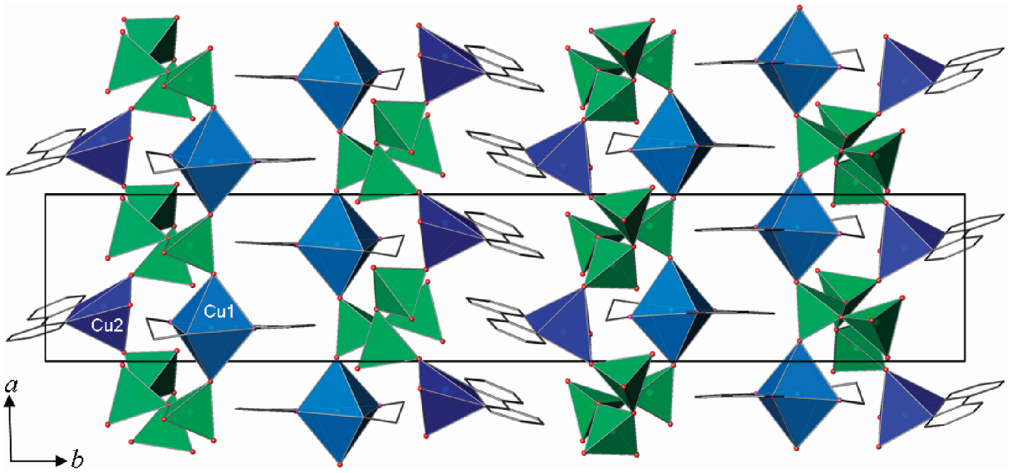

Figure 6. Two different types of $\pi-\pi$ stacking alternating in the structure, between octahedral copper atoms (Cu1, light blue) and between pentacoordinated copper atoms (Cu2, dark blue). Vanadium(V) is shown as green tetrahedra.

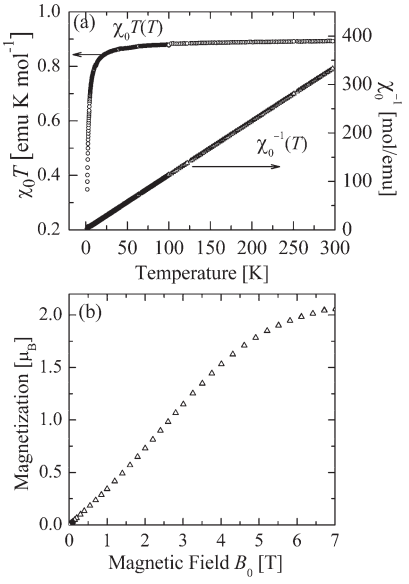

Figure 7. (a) $\chi_0 T$ (T) (left) and $\chi_0^{-1}(T)$ (right) for an applied field of 1 T. The solid line for $\chi_0^{-1}(T)$ between 100 and 300 K corresponds to the linear regression analysis used to obtain a Weiss constant of $\theta = -2$ K. (b) Isothermal magnetization curve $M(B_0)$ observed at $T = 1.8$ K.

of the scarce information that exists regarding the problem, it is difficult to argue about their relative role in supporting exchange coupling interactions. Therefore, in the discussion that follows, and to evaluate $|J_4|$ from the EPR results, it will be assumed without strong arguments, equal contributions of both stacking interactions.

Magnetic Results. The susceptibility data related to **1** are displayed as $\chi_0 T$ in Figure 7a, for $B_0 = 1$ T and two copper ions per molecular unit. In the temperature range of 100−300 K, $\chi_0 T$ remains constant and is equal to 0.85 emu mol^{-1} K, and the effective moment is 1.85 μ_B per copper center, indicating a g-factor of $g = 2.14$. $\chi_0 T$ decreases abruptly for T below ca. 20 K, and at 1.82 K, it is $\chi_0 T = 0.41$ emu mol^{-1} K, indicating predominant antiferromagnetic interactions at low temperatures. The observed isothermal magnetization curve at 1.8 K displayed in Figure 7b as a function of the magnetic field tends to a value of 2 μ_B at high fields, as expected for two copper ions per molecular unit.

According to the previous analysis of the exchange pathways, we assume that the magnitude of the exchange interaction J_1 for the chains of Cu1 spins is similar to J_2 for the Cu2 spins, and that the effect on the magnetic susceptibility of J_3 and J_4 between Cu1 and Cu2 ions is negligible. In the high-temperature range, we use the Curie−Weiss law:[41]

$$\chi(T) = \frac{Ng^2\mu_B^2 S(S+1)}{3k\left(T - \frac{zJS(S+1)}{3k}\right)} = \frac{C}{T-\theta}$$

where the exchange coupling parameter J is defined by[41] $\mathscr{H}_{ex}(i,j) = J_{ij}S_iS_j$ and, in the molecular field approximation, the Curie and Weiss constants:[41] $C = \frac{Ng^2\mu_B{}^2S(S+1)}{3k}$ $\theta = \frac{zJS(S+1)}{3k}$. Linear regression of the susceptibility data in the range of 100−300 K allowed calculation of the values $\theta = -2$ K (see Figure 7a) and $C = 0.9$ (two coppers per molecule), indicating a g-value of 2.19. Assuming that the coupling interactions of a copper ion with its four nearest Cu neighbors ($z = 4$) are similar, and using the molecular field approximation,[41] one obtains $J = -1.4$ cm^{-1} for the average antiferromagnetic interaction with copper neighbors in the layer. With the same assumptions, and considering now the susceptibility data in the low-temperature range (1.8−50 K), a regular spin chain model was used to estimate the mean J-value. The polynomial approximation of Hatfield,[45] obtained from the predictions of the model of Bonner and Fisher[46] for finite chains of 11 spins $^1/_2$, as reformulated by Kahn,[41] was used to fit the susceptibility data.[47,48] Following this procedure, we obtained $J = -1.7$ cm^{-1} and an average g-factor equal to 2.19 from the low-temperature susceptibility data; these values are similar to the results from the molecular field approximation. The experimental values of $\chi_0 T$ (T) at $T < 50$ K and those calculated with the chain model with $J = -1.7$ cm^{-1} and $g = 2.19$ are shown in Figure 8. Using susceptibility data in the low-temperature range to fit the linear chain model eliminates problems with calculations of temperature-independent corrections that are important and difficult to evaluate with the necessary accuracy. In summary, these arguments support that the mean field approximation and the infinite chain model give similar results and reduce the system to a one-dimensional (1D) magnetic structure.

dx.doi.org/10.1021/ic201278a |*Inorg. Chem.* 2011, 50, 11461–11471

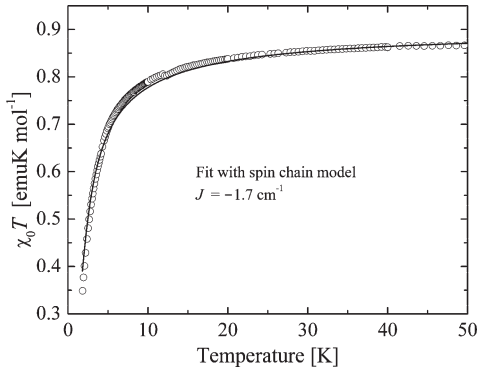

Figure 8. Experimental values of $\chi_0 T$ (T) below 50 K (represented by circles) and values calculated with the method of Bonner and Fisher,[46] as used by Hatfield[45] (represented by the line), described in the text.

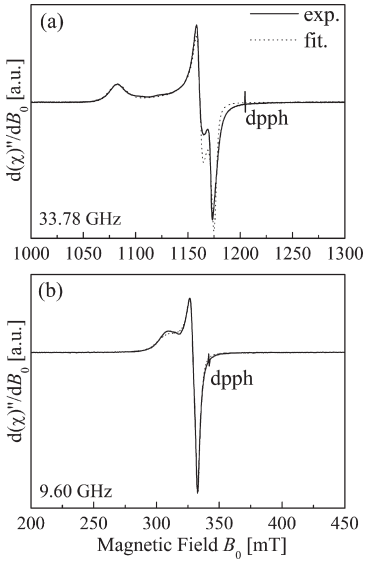

Figure 9. EPR spectra of a powder sample of **1** obtained at 300 K at (a) 33.78 and (b) 9.60 GHz. Solid and dotted lines are, respectively, the experimental results, and the simulations obtained using the parameters given in Table 4a.

EPR Results. *Spectra of a Powder Sample.* EPR spectra of a powder sample of **1** obtained at 33.78 and 9.60 GHz are displayed as solid lines in Figures 9a and 9b, respectively. As it occurs in cases where the copper ions are exchange-coupled, the hyperfine coupling is absent, averaged out by these interactions.[49] The spectrum corresponds to an $S = {}^1/_2$ spin in an axial coordination with a rhombic distortion, response of the *crystal* to the rf excitation. Global fitting of a spin-Hamiltonian for a single species of spin ${}^1/_2$ with an anisotropic $\boldsymbol{g}$-matrix,

$$\mathscr{H}_S = \mu_B \mathbf{S} \mathbf{g} \mathbf{B_0} \qquad (1)$$

to these spectra provides the principal values of this "crystal" $\boldsymbol{g}$-matrix and the line widths collected in Table 4a. The spectra calculated with these parameters, shown in dashed lines in Figure 9a and 9b, assume a single resonance where the $\boldsymbol{g}$-matrix, which is an average of those corresponding to Cu1 and Cu2 in the lattice of compound **1**,[49] and the line width anisotropy

Table 4. (a) Components of the g-matrix Obtained by Global Fitting eq 1 to the EPR Spectra of Powder Samples Observed at 33.78 and 9.60 GHz, Assuming a Single Species of Cu Ions in the Lattice, and (b) Components of the Crystal g^2 Matrix Obtained by a Least-Squares Fit of eq 2 to the Data Taken in Single Crystals at 33.92 GHz Displayed in Figure 10[a]

(a) Parameters Obtained from Spectra of Powder Sample

	ν = 33.78 GHz	ν = 9.60 GHz
g_1	2.044(1)	2.058(1)
g_2	2.079(1)	2.082(1)
g_3	2.231(1)	2.227(1)
g_{iso}	2.123(1)	2.124(1)
σ	2.6%	0.8%

(b) Parameters Obtained from the Single-Crystal Spectra (ν = 33.92 GHz)

$(g^2)_{xx}$	4.9598(7)	$(g^2)_{xy}$	∓0.1433(3)
$(g^2)_{yy}$	4.3323(3)	$(g^2)_{zx}$	− 0.0197(1)
$(g^2)_{zz}$	4.2483(9)	$(g^2)_{zy}$	±0.0520(6)
$(g^2)_1$	4.9923(3)	$\boldsymbol{a_1}$	[0.9757(6), ∓0.2151(9), −0.0409(8)]
$(g^2)_2$	4.2201(3)	$\boldsymbol{a_2}$	[0.0729(9), ± 0.4950(9), −0.8658(9)]
$(g^2)_3$	4.3280(3)	$\boldsymbol{a_3}$	[0.2065(9), ± 0.8418(9), 0.4987(9)]

[a] $(g^2)_1$, $(g^2)_2$, $(g^2)_3$ and $\boldsymbol{a_1}$, $\boldsymbol{a_2}$, $\boldsymbol{a_3}$ are the eigenvalues and eigenvectors of the $\boldsymbol{g^2}$-matrix. In this fitting, we assume two symmetry-related species of Cu ions in the lattice, and we do not consider the spectra observed in the angular ranges of the *ab* and *c*b* planes, where the two resonances merge. σ is the root-mean-square (rms) deviation of the calculated spectra from the experimental result.

have the same principal axes. This simplification in the simulation may contribute to the discrepancies between observed and simulated spectra around B_0 ~1.17 T, at 33.78 GHz when the resolution is highest (Figure 9a). Other contributions to the discrepancies are discussed later. The $\boldsymbol{g}$-values calculated from the data (Table 4a) are in good agreement with those calculated from the susceptibility data and reveal the rhombic distortion of the g-matrix previously mentioned.

Single-Crystal EPR Spectra. The angular variation of the EPR spectra observed at 33.92 GHz displays a rich and interesting behavior. A single EPR line was observed for any orientation of $\boldsymbol{B_0}$ in the *c*a* plane, while one or two resonances were observed for different orientation ranges of $\boldsymbol{B_0}$ in the *ab* and *c*b* planes. In fact, the two peaks observed in these planes merge into one near the axes. No hyperfine structure due to the nuclear spin of copper was observed at any magnetic field orientation. Positions and peak-to-peak line widths (ΔB_0) of the resonance lines were obtained by least-squares fits of one or two Lorentzian derivative lines of the spectra, according to the observed result. Smaller angular intervals (1°) were used in the angular ranges of the *ab* and *c*b* planes, where the collapse of two resonances to a single line occurs. Figures 10a−c and 11a−c, respectively, display the angular variations of the squared g-factor and the line widths of the resonances, observed for $\boldsymbol{B_0}$ in the three studied planes. Considering the data in the *ab* and *c*b* planes for orientations where two resonances are observed, and the data in the *c*a* plane, where one line is observed for any orientation of B_0 for symmetry conditions (see later), we used a least-squares method to obtain the matrix elements of g^2 for each resonance

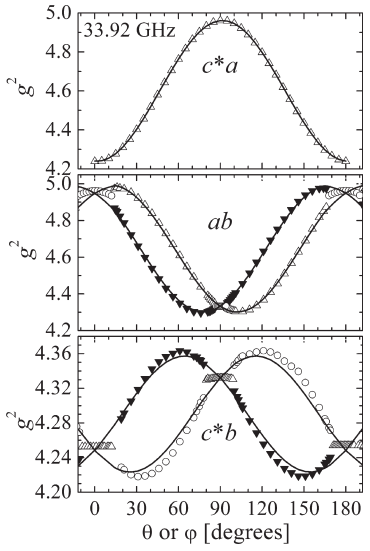

Figure 10. Experimental values of the g^2-factor at 33.92 GHz and 300 K for $\boldsymbol{B}_0$ applied in the three crystal c^*a, ab, and c^*b planes. Symbols are the experimental values. The solid lines were obtained with the components of g^2 given in Table 4b.

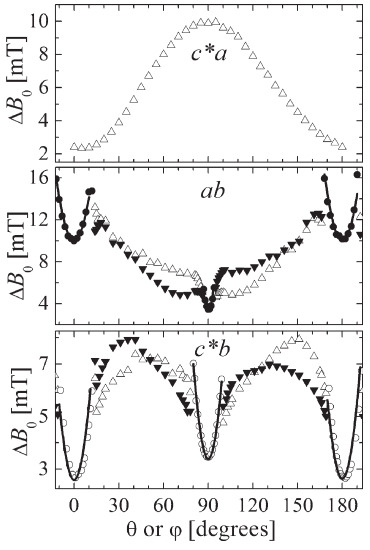

Figure 11. Angular variation of the peak-to-peak line width (ΔB_0) of the resonance observed at 33.92 GHz and 300 K for **1** and $\boldsymbol{B}_0$ applied in the three crystal planes. The solid parabolic lines included in the ab and c^*b planes in the angular ranges, where a single line is observed, are obtained with the model described in the text.

in Figure 10. We used

$$g^2(\theta,\phi) = (g^2)_{xx}\sin^2\theta\cos^2\phi + (g^2)_{yy}\sin^2\theta\sin^2\phi + (g^2)_{zz}\cos^2\theta + 2(g^2)_{xy}\sin^2\theta\sin\phi\cos\phi + 2(g^2)_{xz}\sin\theta\cos\theta\cos\phi + 2(g^2)_{yz}\sin\theta\cos\theta\sin\phi \quad (2)$$

and the values of the parameters obtained are given in Table 4b, which also contains eigenvalues and eigenvectors of these matrices. The predictions of the global fit, indicated as solid lines in Figure 10, are in good agreement with the observed angular variation (except in the angular regions near the axes, where the two peaks merge) and it is important to note that the components of the g^2-matrices evaluated from single-crystal measurements are slightly different from those obtained from simulations of powder spectra, where we proposed a single resonance for all field orientations. This first analysis of the single-crystal data does not consider the collapse of the two peaks near the axes in the ab and c^*b planes that are treated in the next section.

EPR Spectra and Dimensional Phase Transition. Here, we fully interpret the EPR data in single crystals in terms of the structure of the Cu^{II} ions in the compound and of the exchange interactions network that couples them, which was described previously. The EPR signals observed in **1** are the response to the microwave field of the copper ions. Each asymmetric cell of **1** contains two chemically different copper atoms, Cu1 and Cu2, and repeats four times in the unit cell at positions A = (x, y, z), B = $(-x + {}^1/_2, y + {}^1/_2, -z + {}^1/_2)$, C = $(-x, -y, -z)$; D = $(x - {}^1/_2, -y - {}^1/_2, z - {}^1/_2)$, related by C_2 rotation operations and by inversions, plus a displacement. In the absence of exchange couplings between Cu ions, and because of the space symmetry of **1**, one should observe four EPR signals for a general orientation of the field B_0, two corresponding to Cu1 and Cu2 ions at layers type A, and other two corresponding to these ions at layers type B, differing from layer A by a rotation of 180° around the $\boldsymbol{b}$-axis. Copper spins related by inversion operations at layers A and C, and B and D, give rise to signals identical to those previously described.

The exchange coupling interactions between copper ions change this view, adding new interesting features to the EPR data. According to the stochastic theory of narrowing and collapse of magnetic resonance lines introduced by Anderson,[50,51] when the magnitude of the exchange coupling J between two different spin species is larger than the distance between their individual resonances, the two resonances merge into a single one, with behavior described by the theory. Only the magnitudes $|J|$ of these couplings are relevant in this phenomenon, and no information on the sign of the interactions can be obtained. The main hypothesis of this theory is that the interaction J of a spin with its environment has a stochastic distribution, as occurs in an infinitely sized material (an infinite-body problem). These ideas have been used to estimate very weak exchange interactions between metal ions in solids of the order of ~0.001 cm^{-1}, even when much larger interactions exist simultaneously in the system, as discussed in previous publications.[27−29,52−55]

The exchange couplings J_1 and J_2 defined above between Cu1 neighbors, and between Cu2 neighbors in a chain, respectively, do not change this view, and are irrelevant to the EPR spectra, because they couple identical spins and the isotropic exchange coupling commutes with the Zeeman coupling. In such a case, one should observe a spectrum corresponding to Cu1 and another corresponding to Cu2. However, if the exchange coupling $|J_3|$ between Cu1 and Cu2 neighbors within a layer is large enough, the signals from these two ions collapse into one signal, and only one peak is observed for each layer: one for Cu1 + Cu2 in layers A + C and the other for Cu1 + Cu2 in layers B + D.[27,54] In that case, the wave function of the unpaired spin is delocalized over the layer with a $\boldsymbol{g}$-matrix equal to the crystal $\boldsymbol{g}$-matrix introduced in eq 1. This delocalization is also caused by the fact that the hyperfine structure is washed out,[56] as it is observed for **1**. If, in addition, the interaction $|J_4|$ between copper atoms in neighboring layers is large enough, only one exchange collapsed

signal is observed. This is the model that we present below, and is used to evaluate the interactions $|J_3|$ and $|J_4|$. The single-crystal EPR data displayed in Figures 10 and 11 gives information about these two smallest couplings between neighboring copper atoms of different types in the lattice. The two signals observed in the planes *ab* and *c**b* correspond to layers A and C, and B and D, respectively. A merging into one of the resonances corresponding to the different layers occurs near the axes when the interlayer coupling becomes larger than the energy difference involved in the transition. The coupling $|J_4|$ is fixed, but we sweep through this condition, changing the positions of the peaks with magnetic field orientation. For the range of orientations of $\boldsymbol{B_0}$ where two signals are observed, compound **1** behaves as a two-dimensional (2D) magnetic system and each signal is assigned to a copper layer. In the range of field orientations where only one resonance is observed, the behavior is three-dimensional (3D); i.e., according the EPR measurement, the interlayer coupling is large enough (compared with the energy splittings) to change the magnetic dimensionality of the system to three dimensions.

The merging of two signals into a single one, as a consequence of the exchange interactions previously described, is a quantum phase transition that occurs when the magnitude of the root-mean-square (rms) interaction between neighbor spins in different environments becomes larger than the energy splitting of the EPR transitions involved. This phenomenon occurs as a transition between two well-defined quantum states and also occurs for materials with weakly interacting dinuclear units.[31,57,58] Wave functions, which, for a small interaction $|J_3|$ would be localized in one of the two copper atoms (Cu1 or Cu2), in the presence of a sufficiently strong interaction, delocalize to an extended wave function with a finite amplitude on each ion and with properties that are the average of the individual values. In our experiments at 33.92 GHz, the peaks of Cu1 and Cu2 are merged for any field orientation. To break this condition, it would be necessary to perform measurements at higher microwave frequencies. Our experiments only allow obtaining a lower limit for $|J_3|$. Similar reasoning can be made for $|J_4|$; when it is smaller than the line splitting, each copper layer gives its own signal. However, in that case, we can sweep through the merging condition with magnetic field orientation and the position of the transition allows one to obtain a well-defined value for $|J_4|$. Figure 12 shows the ratio $\Delta g_{exp}/\Delta g_{calc}$ in the *ab* and *c**b* planes plotted against the quantity $(\mu_B \Delta g_{calc} B_0)^{-1}$ in units of cm

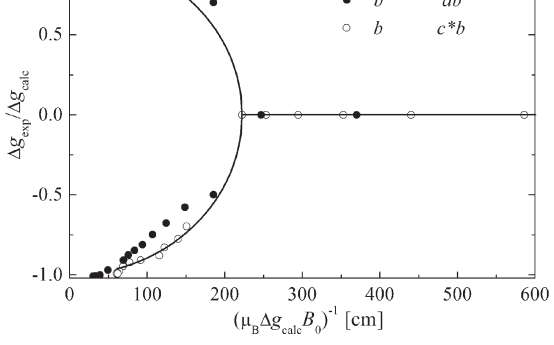

Figure 12. Collapse of the resonances as a function of the inverse of the line splitting around the *b*-axis in the *ab* and *c**b* planes. The collapse of the signals is a function of the root-mean-square (rms) average of the exchange coupling between Cu ions in neighboring layers.

(inverse energy units, cm^{-1}), with μ_B being the Bohr magneton. Δg_{exp} and Δg_{calc} are calculated from the distances in magnetic field between the two observed lines, and from the calculated distances of the positions obtained from the fits with eq 2, respectively. A value for the exchange frequency $\hbar\omega_{ex}$ = 0.0045 cm^{-1} was obtained by fitting the function[27−30]

$$\frac{\Delta g_{exp}}{\Delta g_{calc}} = \pm\sqrt{1-\left(\frac{\hbar\omega_{ex}}{\mu_B \Delta g_{calc} B_0}\right)^2} \quad (3)$$

to the data in Figure 12. The solid line in this figure, which has been obtained from this fitting, is in good agreement with the experimental data. The exchange frequency (ω_{ex}) in eq 3 was introduced by Kubo[59] and is related to the time correlation function of the spin dynamics produced by exchange coupling. Each contribution to the exchange is associated to a particular exchange frequency ω_{ex} (here, we deal with only one value). Below, we show the relationship between ω_{ex} and the exchange couplings, giving rise to the spin dynamics.

The parabolic dependence of the line width that is observed in the angular regions, where the peaks corresponding to the different layers merge (collapsed regions), provides another way to calculate ω_{ex}. Figures 11a−c display the angular dependence of the EPR peak-to-peak linewidth $\Delta B_0(\theta,\phi)$ observed for $\boldsymbol{B}$ in the crystal planes *ab* and *c**b*. It has been shown that[54]

$$\Delta B_0(\theta,\phi) = \sqrt{\frac{2\pi}{3}}\left(\frac{\omega_0^2\hbar}{\mu_B}\right)\left(\frac{4}{\omega_{ex}}\right)\left[\frac{(\mathbf{h}\cdot\mathbf{g}\cdot\mathbf{G}\cdot\mathbf{h})^2}{g(\theta,\phi)^4}\right] + \Delta B_0(0) \quad (4)$$

where $\boldsymbol{G}$ is defined by Passeggi et al.[54] and accounts for the difference between the average *g*-factors corresponding to the different layers, ΔB_0 is the residual line width along the crystal axes, ω_0 is the Larmor frequency, $\hbar$ is Planck's constant, and μ_B is the Bohr magneton. A least-squares fitting of eq 4 to the linewidth data in the collapsed regions around the *b*-axis in the *ab* and *c**b* planes was performed; the results are shown as solid lines in Figures 11a−c and allow one to obtain $\hbar\omega_{ex}$ = 0.0065 cm^{-1}, similar within the expectancies for the value obtained from Figure 12. The components of the molecular *g*-matrix evaluated above (Table 4), average of the *g*-matrices for Cu1 and Cu2, were used to obtain the exchange frequency whose value is related to the exchange parameter *J* by the following equation:[27,28,30]

$$\hbar\omega_{ex} = \sum_i (z_i J_i^2)^{1/2} \quad (5)$$

where z_i is the number of the nearest neighboring Cu ions connected by the *i*th chemical path and J_i are the exchange parameters associated with each chemical path connecting pairs of copper atoms. Using eq 5, we obtain $|J_4|$ = 0.0034 ± 0.0004 cm^{-1} for the coupling between Cu ions in neighboring layers, using the average ω_{ex} values, from the collapse of the resonances (Figure 12) and from the linewidth data around the axes in the *ab* and *c**b* planes (Figure 11). More details about these calculations can be found in previous papers.[27−31]

Exchange coupling interactions between metal ions supported by the stacking of the rings of pyridine and 1,10-phenanthroline have been estimated in the past from mean field approximation analysis of susceptibility data. Using this methodology, it is difficult

to separate the contribution from different sources of exchange couplings, and the results are crude approximations.[35,36] In a recent publication, Neuman et al.[37] studied by EPR the weak ferromagnetic dinuclear copper compound $[Cu(tda)(phen)]_2 \cdot H_2tda$ (tda = thiodiacetate, phen =1,10-phenanthroline). They analyzed the data using a method discussed by Anderson[51] and by Weil et al.,[60] where the exchange frequency is calculated from fits of this method to the resonances observed in the angular region where two peaks are observed. They reported $J' = 0.0070\ cm^{-1}$ for the coupling between units, which they claim to be supported by the stacking of phenanthroline rings. This value is very close to our result, even though the characteristics of the reported compound[37] introduce higher restrictions to separate the effect of the interactions present in the system in the analysis of the EPR data. In our work, Figures 11 and 12 allow a much more direct way to evaluate the coupling. Comparison of the results indicate that the stacking of phenanthroline and bipyridine molecules produces similar coupling interactions.

CONCLUSIONS

This work provides a new example of oxovanadium−copper bipyridine hybrid organic−inorganic compound, which presents two different Cu^{II} centers, in penta- and hexa-coordination modes. The compound shows two different $\pi-\pi$ stacking interactions in the crystal lattice.

Similar results were obtained by modeling the magnetic measurements with the mean field Curie−Weiss approximation and with a quantum model considering spin chains arranged in layers, supporting the idea of isolated spin chains, with an average antiferromagnetic coupling between nearest-neighboring copper ions $J = -1.6\ cm^{-1}$.

Cu1 and Cu2 ions in neighboring chains are coupled by weaker exchange interactions with $|J_3| > 0.04\ cm^{-1}$, which are important to describe the behavior of the EPR spectra in oriented single crystals. The most relevant electron paramagnetic resonance (EPR) results refer to the layered structure of the copper ions and the role of the stacked structures of bipy molecules, acting as path for superexchange interactions (J_4) between copper atoms in neighboring layers at ca. 10 Å.

The coupling interactions described by J_3 and J_4 produce a quantum phase transition where the wave functions of the Cu ions, localized principally on the individual Cu centers, change to be localized in layers containing Cu1 and Cu2 ions due to J_3, and to be delocalized in 3D due to the interlayer coupling J_4. This last transition allows one to estimate an average value $|J_4| = 0.0034 \pm 0.0004\ cm^{-1}$. These transitions are observed as the merging of the EPR peaks of the single-crystal spectra of **1** produced by the different exchange interactions between copper atoms.

In the case of J_1, J_2, and J_3, the exchange pathways involve one or more ···O−V−O··· covalent units; however, J_4 is a consequence of the coupling through the stacking of the bipy rings that separate the copper layers at ca. 10 Å in the compound.

In conclusion, EPR provides a very sensitive tool to evaluate very weak interactions between metal ions, even in the presence of much-larger exchange couplings.

ASSOCIATED CONTENT

Supporting Information. This material is available free of charge via the Internet at http://pubs.acs.org.

AUTHOR INFORMATION

Corresponding Author

*E-mail: diego.venegas@usach.cl.

ACKNOWLEDGMENT

The authors from Chile thank FONDECYT for partial financial support (through Project Nos. 1080316, 1080318, and 1080234, as well as Financiamiento Basal Program FB0807). They also thank the DFG-CONICYT Collaborative Program. This work was done under the LIA-MIF 836 International Collaboration Program (CONICYT-CNRS). K.A.B. thanks CONICYT for the doctoral scholarships (Nos. 21050162 and AT-24071044) and the University of Chile for the AVV-5 grant. This work was supported by CNPQ in Brazil and by CAI+D-UNL in Argentina. R.C. is a member of CONICET, Argentina.

REFERENCES

(1) Muller, A.; Peters, F.; Pope, M. T.; Gatteschi, D. *Chem. Rev.* **1998**, *98*, 239–271.
(2) Thomas, J.; Sharma, S.; Lofland, S. E.; Ramanujachary, K. V.; Ramanan, A. *J. Chem. Sci.* **2006**, *118*, 79–86.
(3) Wang, L.; Sun, X.-P.; Liu, M.-L.; Gao, Y.-Q.; Gu, W.; Liu, X. *J. Cluster Sci.* **2008**, *19*, 531–542.
(4) Zheng, L.-M.; Zhao, J.-S.; Lii, K.-H.; Zhang, L.-Y.; Liu, Y.; Xin, X.-Q. *J. Chem. Soc., Dalton Trans.* **1999**, 939–944.
(5) Ouellette, W.; Burkholder, E.; Manzar, S.; Bewley, L.; Rarig, R. S.; Zubieta *J. Solid State Sci.* **2004**, *6*, 77–84.
(6) Xie, J.-Y.; Mao, J.-G. *J. Mol. Struct.* **2005**, *750*, 186–189.
(7) Manzur, J.; Mora, H.; Vega, A.; Spodine, E.; Venegas-Yazigi, D.; Garland, M. T.; Salah El Fallah, M.; Escuer, A. *Inorg. Chem.* **2007**, *46*, 6924–6932.
(8) Ushak, S.; Spodine, E.; Le Fur, E.; Venegas-Yazigi, D.; Pivan, J. Y.; Schnelle, W.; Cardoso-Gil, R.; Kniep, R. *Inorg. Chem.* **2006**, *45*, 5393–5398.
(9) Spodine, E.; Venegas-Yazigi, D.; Ushak, S.; Paredes-García, V.; Saldías, M.; Le Fur, E.; Pivan, J. Y. *Polyhedron* **2007**, *26*, 2121–2125.
(10) Paredes-Garcia, V.; Gaune, S.; Saldías, M.; Garland, M. T.; Baggio, R.; Vega, A.; Salah El Fallah, M.; Escuer, A.; Le Fur, E.; Venegas-Yazigi, D.; Spodine, E. *Inorg. Chim. Acta* **2008**, *361*, 3681–3689.
(11) Ushak, S.; Spodine, E.; Venegas-Yazigi, D.; Le Fur, E.; Pivan, J. Y. *Microporous Mesoporous Mater.* **2006**, *94*, 50–55.
(12) Li, T.; Liu, J.; Gao, S.; Li, F.; Kao, R. *Chem. Lett.* **2007**, *36*, 356–357.
(13) Le Fur, E.; Pivan, J. Y.; Ushak, S.; Venegas-Yazigi, D. *Inorg. Chim. Acta* **2008**, *361*, 1891–1896.
(14) Zhang, Y.; Clearfield, A.; Haushalter, R. *J. Solid State Chem.* **1995**, *117*, 157–164.
(15) Shi, Z.; Feng, S.; Zhang, L.; Yang, G.; Hua, J. *Chem. Mater.* **2000**, *12*, 2930–2935.
(16) Finn, R. C.; Zubieta, J. *J. Phys. Chem. Solids* **2001**, *62*, 1513–1523.
(17) Wang, C.-M.; Lii, K.-H. *J. Solid State Chem.* **2003**, *172*, 194–199.
(18) Zhang, X.-M.; Wu, H.-S.; Gao, S.; Chen, X.-M. *J. Solid State Chem.* **2003**, *176*, 69–75.
(19) Moreno, Y.; Vega, A.; Ushak, S.; Baggio, R.; Peña, O.; Le Fur, E.; Pivan, J.-Y.; Spodine, E. *J. Mater. Chem.* **2003**, *13*, 2381–2387.
(20) Cui, Y.; Li, G.; Meng, H.; Xing, Y.; Ding, H.; Sun, J.; Liu, L.; Pang, W. *Inorg. Chem. Commun.* **2004**, *7*, 909–911.
(21) Wang, C.-M.; Chuang, Y.-L.; Chuang, S.-T.; Lii, K.-H. *J. Solid State Chem.* **2004**, *177*, 2305–2310.
(22) Koo, B.-K.; Ouellette, W.; Burkholder, E. M.; Golub, V.; O'Connor, C. J.; Zubieta *J. Solid State Sci.* **2004**, *6*, 461–468.
(23) Ushak, S.; Spodine, E.; Venegas-Yazigi, D.; Le Fur, E.; Pivan, J. Y.; Peña, O.; Cardoso-Gil, R.; Kniep, R. *J. Mater. Chem.* **2005**, *15*, 4529–4534.

(24) Cui, Y.; Meng, H.; Liu, L.; Li, G.; Chen, C.; Yi, Z.; Pang, W. *Solid State Sci.* **2006**, *8*, 1108–1114.
(25) Spodine, E.; Venegas-Yazigi, D.; Ushak, S.; Le Fur, E.; Pivan, J. Y. *Physica B* **2006**, *384*, 120–122.
(26) (a) Calvo, R.; Rapp, R. E.; Chagas, E.; Sartoris, R. P.; Baggio, R.; Garland, M. T.; Perec, M. *Inorg. Chem.* **2008**, *47*, 10389–10397. (b) Calvo, R.; Rapp, R. E.; Sartoris, R. P.; Santana, R. C.; Perec, M. *J. Phys. Chem. A* **2009**, *113*, 8830–8833.
(27) (a) Martino, D. M.; Passeggi, M. C. G.; Calvo, R. *Phys. Rev. B* **1995**, *52*, 9466–9476. (b) Calvo, R.; Isern, H.; Mesa, M. A. *Chem. Phys.* **1985**, *100*, 89–99.
(28) Martino, D. M; Passeggi, M. C. G.; Calvo, R.; Nascimento, O. R. *Physica B* **1996**, *225*, 63–75.
(29) (a) Costa-Filho, A. J.; Munte, C. E.; Barberato, C.; Castellano, E. E.; Mattioli, M. P. D.; Calvo, R.; Nascimento, O. R. *Inorg. Chem.* **1999**, *38*, 4413–4421. (b) Costa-Filho, A. J.; Nascimento, O. R.; Ghivelder, L.; Calvo, R. *J. Phys. Chem B* **2001**, *105*, 5039–5047.
(30) Calvo, R. *Appl. Magn. Reson.* **2007**, *31*, 271–299.
(31) Napolitano, L. M. B.; Nascimento, O. R.; Cabaleiro, S.; Castro, J.; Calvo, R. *Phys. Rev. B* **2008**, *77*, 214423–13.
(32) Brondino, C. D.; Calvo, R.; Atria, A. M.; Spodine, E.; Nascimento, O. R.; Pena, O. *Inorg. Chem.* **1997**, *36*, 3183–3189.
(33) Yu, L.; Shi, J. M.; Zhang, Y. Q.; Wang, Y. Q.; Fan, Y. N.; Zhang, G.-Q.; Shi, W.; Cheng, P. *J. Mol. Struct.* **2011**, *987*, 138–143.
(34) (a) Calvo, R.; Abresch, E. C.; Bittl, R.; Feher, G.; Hofbauer, W.; Isaacson, R. A.; Lubitz, W.; Okamura, M. Y.; Paddock, M. L. *J. Am. Chem. Soc.* **2000**, *122*, 7327–7341. (b) Calvo, R.; Isaacson, R. A.; Paddock, M. L.; Abresch, E. C.; Okamura, M. Y.; Maniero, A.-L.; Brunel, L.-C.; Feher, G. *J. Phys. Chem. B* **2001**, *105*, 4053–4057.
(35) Brondino, C. D.; Calvo, R.; Atria, A. M; Spodine, E.; Peña, O. *Inorg. Chim. Acta* **1995**, *228*, 261–266.
(36) Zhang, J.-W.; Wang, H.-S.; Song, Y. *Inorg. Chem. Commun.* **2011**, *14*, 56–60.
(37) Neuman, N. I.; Perec, M.; González, P. J.; Passeggi, M. C. G.; Rizzi, A. G.; Brondino, C. D. *J. Phys. Chem. A* **2011**, *114*, 13069–13075.
(38) *SAINTPLUS V6.22*; Bruker AXS, Inc.: Madison, WI.
(39) Sheldrick, G. M. *SHELXTL NT/2000, Version 6.10*; Bruker AXS, Inc.: Madison, WI, 2000.
(40) *SADABS V2.05*; Bruker AXS, Inc.: Madison, WI.
(41) Kahn, O. *Molecular Magnetism*; VCH: New York, 1993.
(42) Gennaro, A. M.; Levstein, P. R.; Steren, C. A.; Calvo, R. *Chem. Phys.* **1987**, *111*, 431–438.
(43) Stoll, S.; Schweiger, A. *J. Magn. Reson.* **2006**, *178*, 42–55.
(44) *Matlab*; The Mathworks, Inc.; Natick, MA.
(45) Hatfield, W. E. *J. Appl. Phys.* **1981**, *52*, 1985–1990.
(46) Bonner, J.; Fisher, M. *Phys. Rev.* **1964**, *135*, A640–A658.
(47) Calvo, R.; Levstein, P. R.; Castellano, E. E.; Fabiane, S. M.; Piro, O. E.; Oseroff, S. B. *Inorg. Chem.* **1991**, *30*, 216–220.
(48) Sartoris, R. P.; Santana, R. C.; Baggio, R. F.; Peña, O.; Perec, M.; Calvo, R. *Inorg. Chem.* **2010**, *49*, 5650–5657.
(49) Calvo, R.; Mesa, M. A.; Oliva, G.; Zukerman-Schpector, J.; Nascimento, O. R.; Tovar, M.; Arce, R. *J. Chem. Phys.* **1984**, *81*, 4584–4591.
(50) Anderson, P. W.; Weiss, P. R. *Rev. Mod. Phys.* **1953**, *25*, 269–276.
(51) Anderson, P. W. *J. Phys. Soc. Jpn.* **1954**, *9*, 316–339.
(52) Levstein, P. R.; Calvo, R. *Inorg. Chem.* **1990**, *29*, 1581–1583.
(53) Brondino, C. D.; Casado, N. M. C.; Passeggi, M. C. G.; Calvo, R. *Inorg. Chem.* **1993**, *32*, 2078–2084.
(54) Passeggi, M. C. G.; Calvo, R. *J. Magn. Reson. A* **1995**, *114*, 1–11.
(55) Santana, R. C.; Cunha, R. O.; Carvalho, J. F.; Vencato, I.; Calvo, R. *J. Inorg. Biochem.* **2005**, *99*, 415–423.
(56) (a) Nordio, P. L.; Soos, Z. G.; McConnell, H. M. *Annu. Rev. Phys. Chem.* **1966**, *17*, 237–260. (b) Soos, Z. G. *J. Chem. Phys.* **1966**, *44*, 1729–1733.
(57) Perec, M.; Baggio, R.; Sartoris, R. P.; Santana, R. C.; Peña, O.; Calvo, R. *Inorg. Chem.* **2010**, *49*, 695–703.
(58) Calvo, R.; Abud, J. E.; Sartoris, R. P.; Santana, R. C. *Phys. Rev. B* **2011**, *84*, 104433.
(59) (a) Kubo, R.; Tomita, K. *J. Phys. Soc. Jpn.* **1954**, *9*, 888–919. (b) Kubo, R. In *Stochastic Processes in Chemical Physics*; Schuler, K. E., Ed.; Advances in Chemical Physics, Vol. XV; Wiley: New York, 1969; pp 101−127.
(60) Weil, J. A.; Bolton, J. R. *Electron Paramagnetic Resonance: Elementary Theory and Practical Applications*; Wiley−Interscience: New York, 2007.